

The effect of angular distortion on the fatigue behavior of non-penetrating laser welded lap specimens of 301LN stainless steel

Xiangzhong Guo¹, Wei Liu², Xiqing Li², and Zhikun Song²

¹Beijing Jiaotong University

²Affiliation not available

September 16, 2020

Abstract

In this work, the fatigue behaviors of non-penetrating laser welded lap specimens of cold-rolled 301LN austenitic stainless steel were investigated based on experiments and numerical analyses. The experiments showed the unequal-thickness specimens failed in the thicker bottom sheet under low fatigue loads, even though the mean stress in the thinner top sheet was higher, when the applied loads were high enough, the failure location changed from the bottom sheet to the top sheet. This phenomenon could be successfully explained through traction stress analysis considering the effect of angular distortion. However, the equivalent traction stress representation of fatigue data is below the ASME master S-N curve scatter band since the stress exceeds the yield limit of the base metal at low-cycle fatigue regime. The structural strain approach was then used to consider the effect of plastic deformation, and all fatigue data fall into ASME master E-N curve scatter band. This indicates the structural strain approach in conjunction with the master E-N curve is suitable for correlating both low- and high-cycle fatigue data of the non-penetrating laser welded lap specimens.

The effect of angular distortion on the fatigue behavior of non-penetrating laser welded lap specimens of 301LN stainless steel

Xiangzhong Guo*, Wei Liu*, Xiqing Li, Zhikun Song

School of Mechanical, Electronic and Control Engineering, Beijing Jiaotong University, Beijing 100044, China

Correspondence: Xiangzhong Guo and Wei Liu, School of Mechanical, Electronic and Control Engineering, Beijing Jiaotong University, Beijing, 100044, China, E-mail: 16116366@bjtu.edu.cn and weiliu@bjtu.edu.cn

Abstract: In this work, the fatigue behaviors of non-penetrating laser welded lap specimens of cold-rolled 301LN austenitic stainless steel were investigated based on experiments and numerical analyses. The experiments showed the unequal-thickness specimens failed in the thicker bottom sheet under low fatigue loads, even though the mean stress in the thinner top sheet was higher, when the applied loads were high enough, the failure location changed from the bottom sheet to the top sheet. This phenomenon could be successfully explained through traction stress analysis considering the effect of angular distortion. However, the equivalent traction stress representation of fatigue data is below the ASME master S-N curve scatter band since the stress exceeds the yield limit of the base metal at low-cycle fatigue regime. The structural strain approach was then used to consider the effect of plastic deformation, and all fatigue data fall into ASME master E-N curve scatter band. This indicates the structural strain approach in conjunction with the master E-N curve is suitable for correlating both low- and high-cycle fatigue data of the non-penetrating laser welded lap specimens.

Key words: Steel; Welding; Lap joints; Fatigue fracture; Finite element analysis; Fatigue design

1. Introduction

Light weight railway passenger cars made of cold-rolled 301LN austenitic stainless steel have been widely used in subways and intercity express trains¹⁻⁴. Non-penetrating laser lap welding is an assembling method for the side facade panels of passenger cars, which can provide vehicle bodies with a weld-free appearance and improve corrosion resistances^{5,6}.

Fatigue fracture is the primary failure mechanism of welded vehicle bodies, and a few fatigue tests⁷⁻⁹ concerning the laser welded lap specimens have been conducted. Asim et al.⁷ investigated the fatigue behavior of penetrating laser welded lap specimens of equal thickness, and the specimens failed in the top sheet at high-cycle fatigue life due to the weld bead protrusion on the bottom sheet. Ono et al.⁸ conducted fatigue tests on penetrating laser welded lap specimens with different sheet thickness, and the fatigue strength increases with the increase of the sheet thickness. Sindhu et al.⁹ studied the fatigue behavior of non-penetrating laser welded lap specimens, and the specimens failed in thicker non-penetrating bottom sheets at high-cycle fatigue life, even if the nominal stress in the bottom sheets was lower. However, there is no detailed explanation of why the high-cycle fatigue fracture occurred in the thicker bottom sheets. In this study, the similar fatigue fracture mode was observed and the cause was explained.

Fatigue failure is a highly localized phenomenon in welded lap joints and determining the nominal stress is not always possible^{10,11}. Hsu and Albright¹² combined a static stress analysis and the Neuber's rule to predict the fatigue life of laser welded lap joints. Zhang et al.¹³ presented the structural stress solutions based on the outer surface strains of laser welded lap joints. Baumgartner et al.¹⁴⁻¹⁶ investigated the notch stress approaches for the fatigue assessment of laser welded lap thin-walled joints. Wang et al.¹⁷ calculated the fracture mechanics parameter J-integral to correlate the fatigue data of laser welds. Pan et al.^{7,18,19} calculated the global and local stress intensity factor solutions for the pre-existing and kinked cracks to predict the fatigue lives of laser welded lap specimens. Dong²⁰ proposed a traction stress approach for fatigue evaluation of welded joints, which is suitable for the fusion welded joints²¹⁻²⁵ and frictions stir welded joints²⁶. In addition, Dong²⁷ also proposed a structural strain approach to consider the plastic deformation at the location of stress concentration under low-cycle loading conditions. There has been no systematic fatigue assessment for non-penetrating laser welded lap specimens so far.

The angular distortion is produced when the weld bead does not penetrate the full thickness of the plate, even for small heat input^{28,29}. The misalignment cannot be ignored in fatigue assessment because it induces secondary bending loads that might significantly affect the structural stress^{30,31}. According to Lillemäe et al.^{32,33}, the axial misalignment in laser-based welding butt joints caused a significant notch stress increase on the weld root reducing fatigue strength. Oliveira et al.³⁰ investigated the effect of misalignment on stress for laser welded T-joints based on the nonlinear finite element model with angular distortion, and the stress magnification factor increased linearly with the increase of angular distortion and decreased nonlinearly with the increase of nominal stress.

This work investigated the fatigue behaviors of non-penetrating laser welded lap 301LN sheets of different thicknesses. The main objective is to understand the effect of angular distortion on the fatigue fracture behaviors of the specimens. The traction stress was calculated based on the finite element models with and without angular distortion. The structural strain approach was then used to correlate the fatigue data.

2. Experiments and materials

Cold-rolled sheets of 301LN austenitic stainless steel in 0.8 mm, 1.5 mm and 2.0 mm thicknesses were used to prepare welded specimens, and the chemical compositions and mechanical properties are given in Table 1. A solid-state laser with a laser beam diameter of 0.5 mm was used to prepare the laser welded specimens under a shield of 0° side-blown argon with a discharge rate of 30 L/min, and the welding parameters included the welding power of 1.8 kW ~ 2.4 kW, the defocus distance of -1.0 mm ~ +1.0 mm, and the welding speed

of 20 mm/s ~ 30 mm/s. Figure 1 shows a schematic of the laser welded lap specimen, where the t_1 and t_2 are the thicknesses of top and bottom sheets respectively. Four laser welded specimens are numbered by t_1+t_2 as 1.5+1.5, 2.0+2.0, 0.8+1.5, and 0.8+2.0.

TABLE 1 The chemical compositions and mechanical properties of the 301LN sheet

| Chemical compositions (wt. %) |
|-------------------------------|-------------------------------|-------------------------------|-------------------------------|
| C | Si | Mn | P |
| <0.03 | <1.0 | <2.0 | <0.045 |

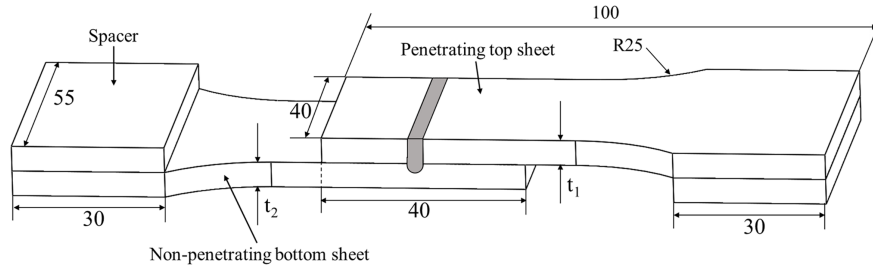


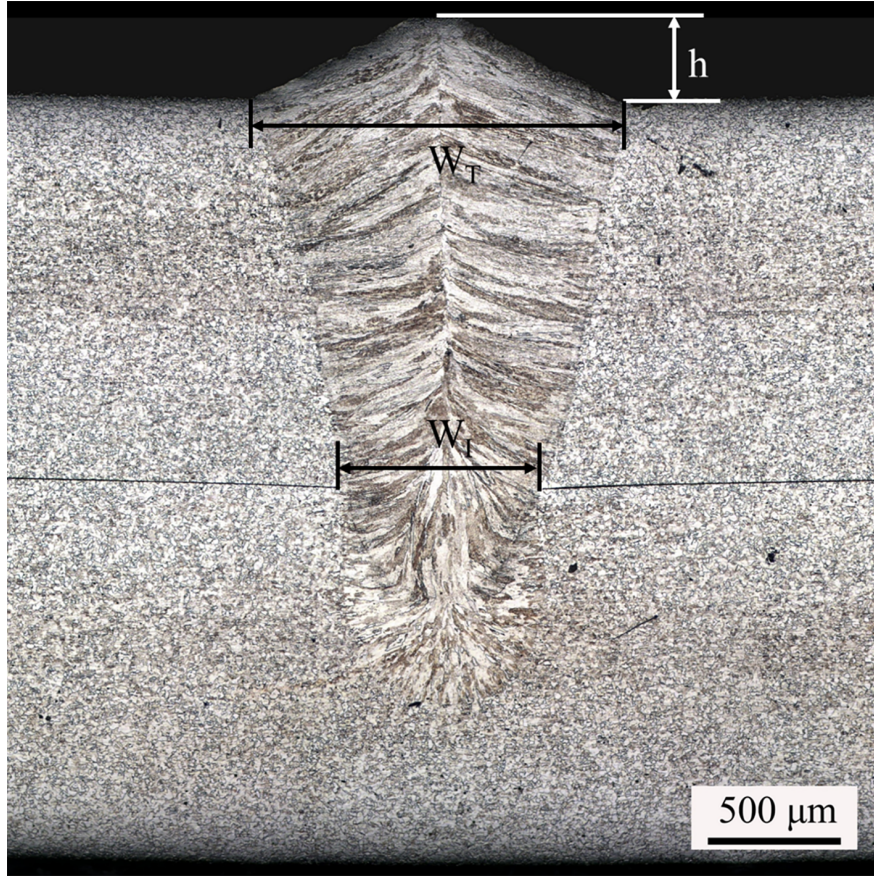
FIGURE 1 A schematic of the laser welded lap specimen (unit mm)

The microstructure of the laser welds was characterized by optical microscope, and Vickers hardness was measured on the transverse cross-section of the laser weld. The angular distortion of welded specimens was measured before the fatigue tests. Fatigue experiments were performed at a frequency of 15 Hz, using sinusoidal-pulse loads with constant amplitudes and a load ratio of $R = 0.1$. Cross-section micrographs of fatigue failure specimens were used to investigate the initiation and propagation of fatigue cracks.

3 Experimental results

3.1 Microstructure and welding distortion

Figure 2 shows the optical micrograph of the cross section of the 1.5+1.5 specimen, and the laser weld appears to be free of thermal cracks and welding porosities. The weld bead was composed of austenite substrate and δ ferrite dendrites spacing less than 10 μm , and the microstructure changes in the heat affected zone is not obvious. Figure 3 shows the microhardness profile of the 1.5+1.5 specimen, and the average hardness of the weld beads is 215 HV and slightly lower than that of the cold-rolled 301LN sheet. The geometric dimensions of the weld beads for four specimens are listed in Table 2, where the parameters are shown in Figure 2.



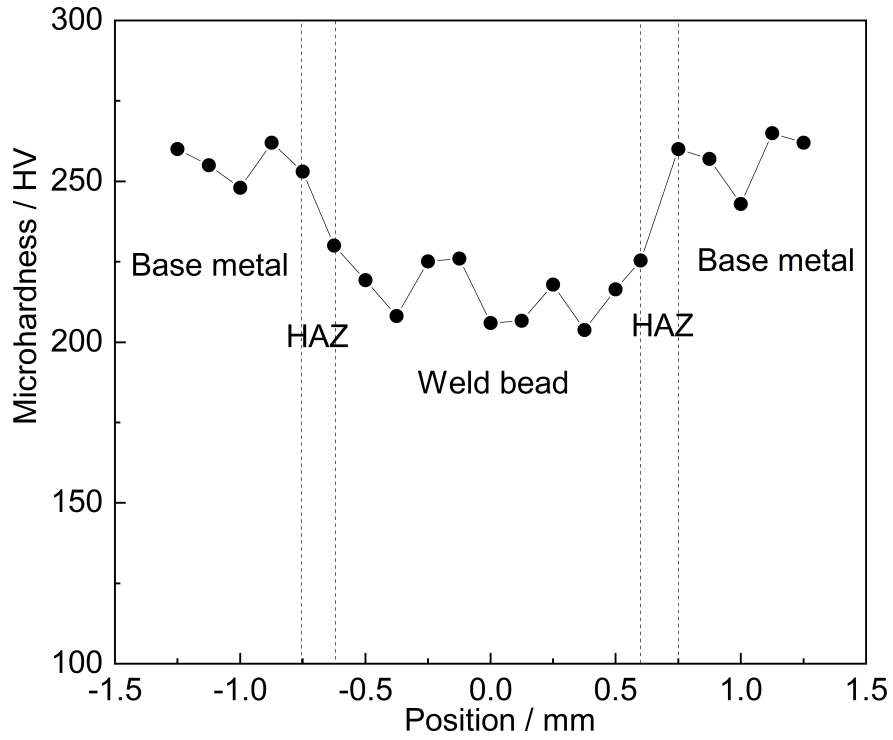


FIGURE 2 Micrographs of the 1.5+1.5 specimen **FIGURE 3**Microhardness profile of the 1.5+1.5 specimen

TABLE 2 Geometric dimensions of the laser welds

Specimens	1.5+1.5	2.0+2.0	0.8+1.5	0.8+2.0
Weld hump h / mm	0.3	0.4	0.2	0.2
Top weld width W_T / mm	1.5	1.8	1.3	1.4
Interfacial weld width W_I / mm	0.85	0.9	0.7	0.8

Figure 4 shows that the angular distortion of the four specimens is less than 1° , and the loading sides are shown by the arrows. The four specimens are tilted upward from the welding center due to the shrinkage of weld beads caused by the uneven welding heat input along the sheet thickness, and the tilt angle of the welded sheet decreases with the increase of sheet thickness.

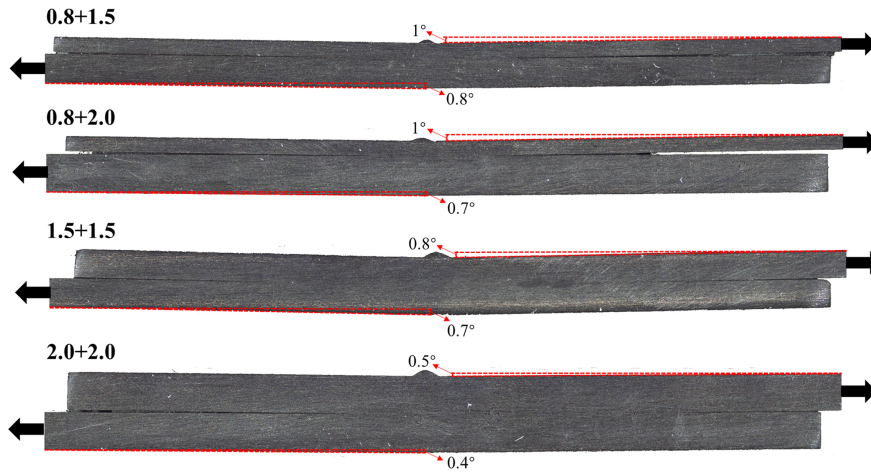


FIGURE 4 Welding angular distortion of four specimens

3.2 Fatigue performance

Figure 5 shows the relationship between the maximum fatigue load and the failure cycle in a log-log scale and the linear fitting for the four specimens, which indicates that the fatigue resistance of the specimen increases with the thickness of lap sheets.

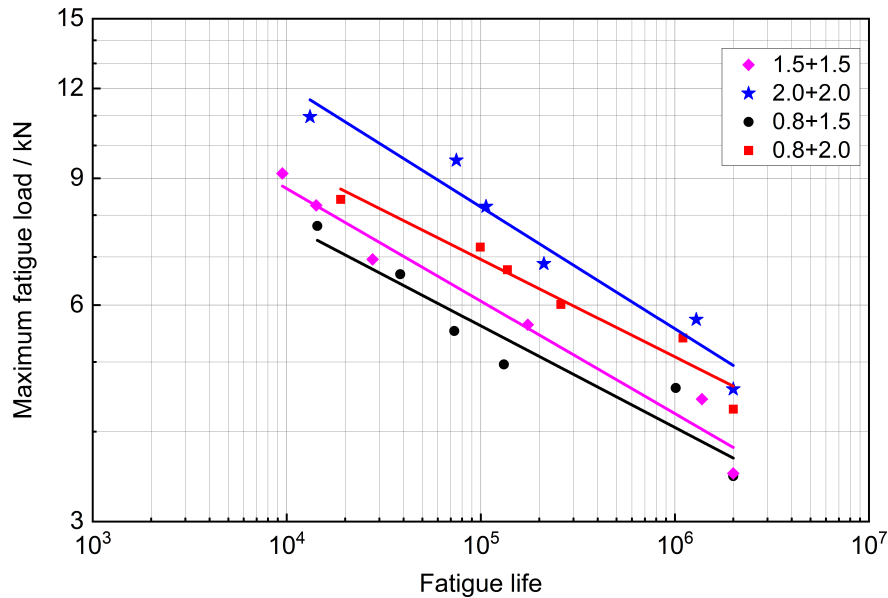
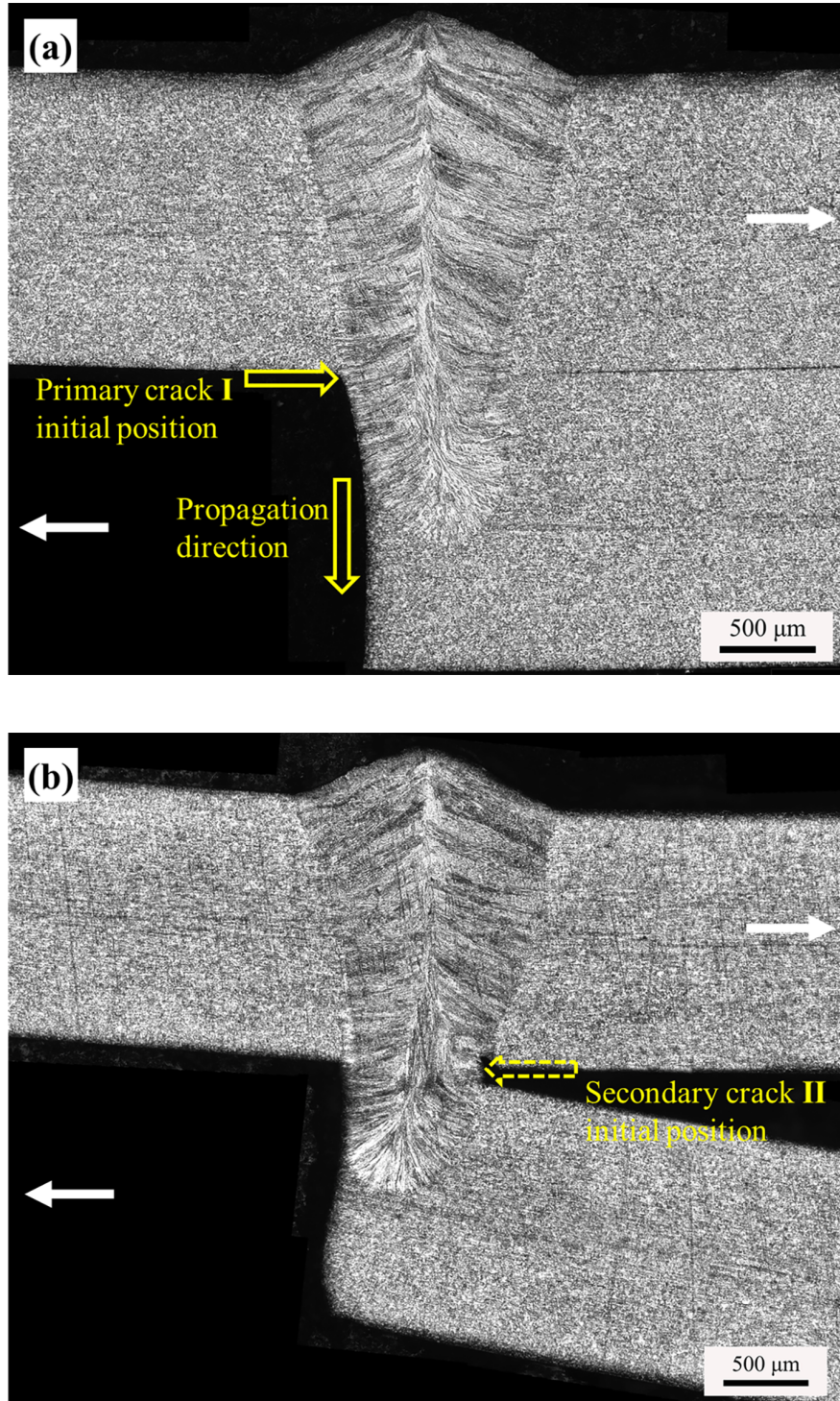
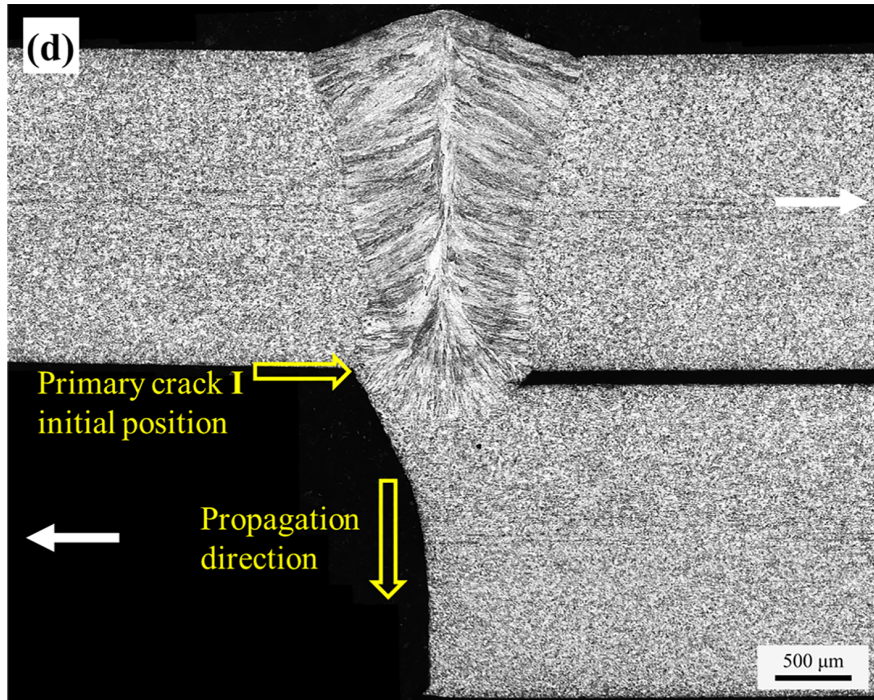
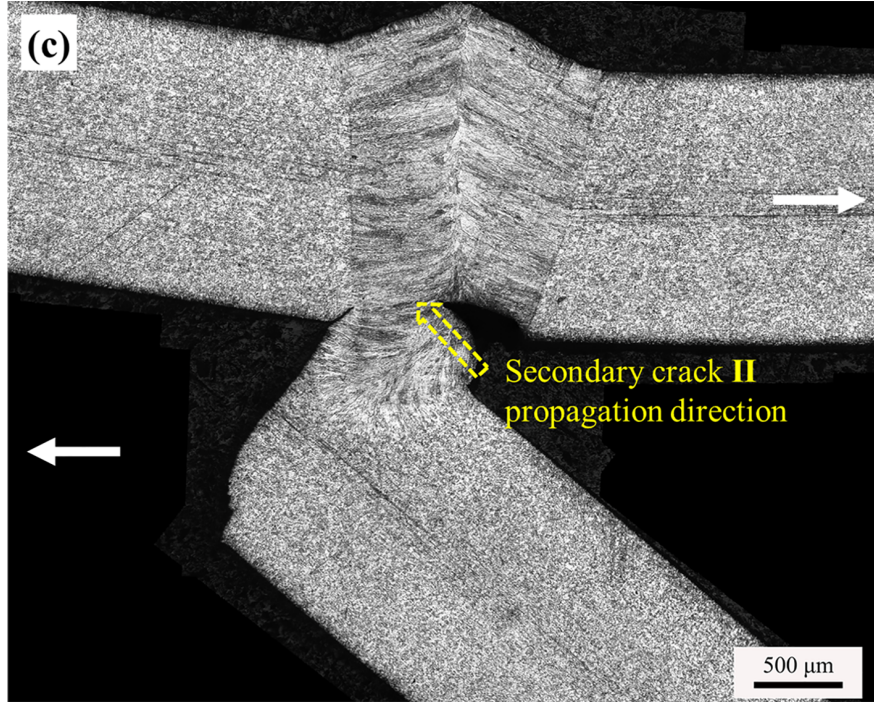


FIGURE 5 Fatigue test results of four specimens

Figure 6 shows cross-section micrographs of fatigue failure 1.5+1.5 and 2.0+2.0 specimens under different fatigue loads, in which loading sides of the top and bottom sheets are shown by the white bold arrows. The specimens of both 1.5+1.5 and 2.0+2.0 failed in the bottom sheet under all fatigue loads, although the mean stress of top and bottom sheets was the same. In addition, as the fatigue loads increase, the laser weld on the top sheet was partially fractured. The fatigue cracks of the lap joint were generally initiated from the notch tips due to its geometry⁷⁻⁹. The primary crack I was initiated from the notch tip on the lap-interface

and propagated through the bottom sheet thickness under low fatigue loads, as shown in Figure 6 (a) and (d). As the fatigue loads increase, the secondary crack II in the top sheet was also initiated from the notch tips as shown in Figure 6 (b) and (e), and propagated along the laser weld dendrite as shown in Figure 6 (c) and (f).





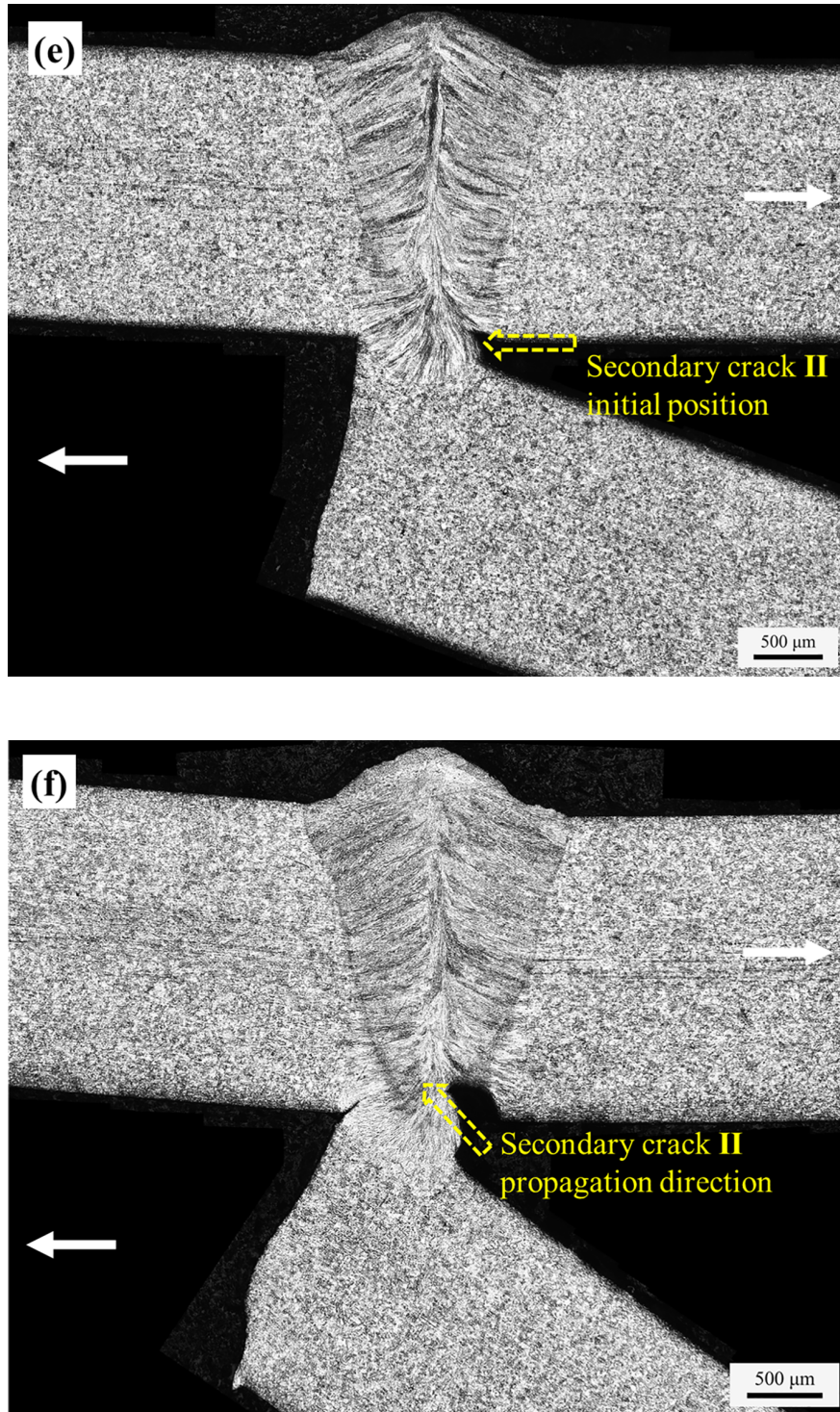
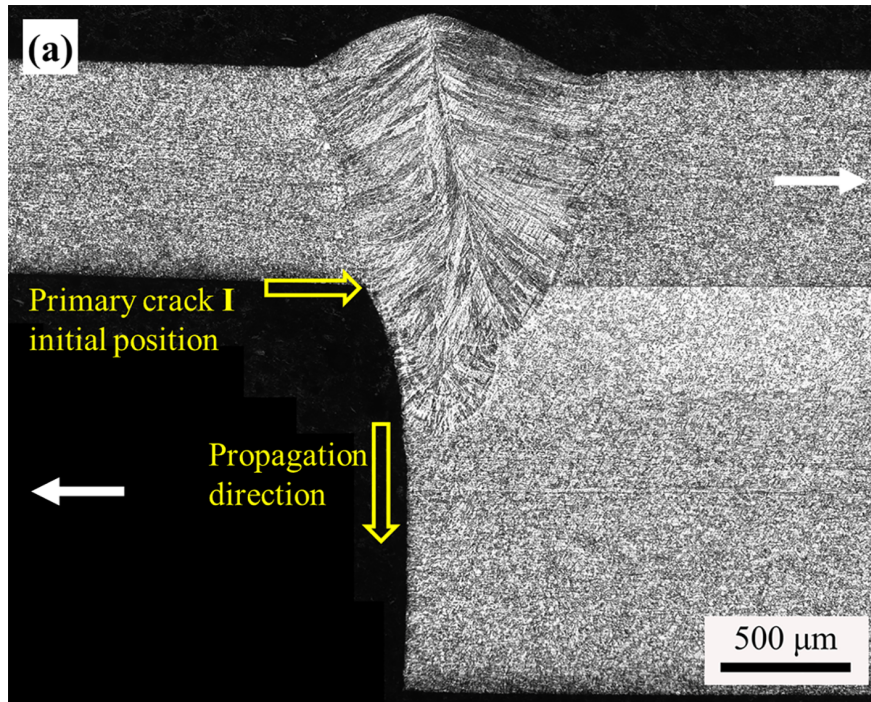
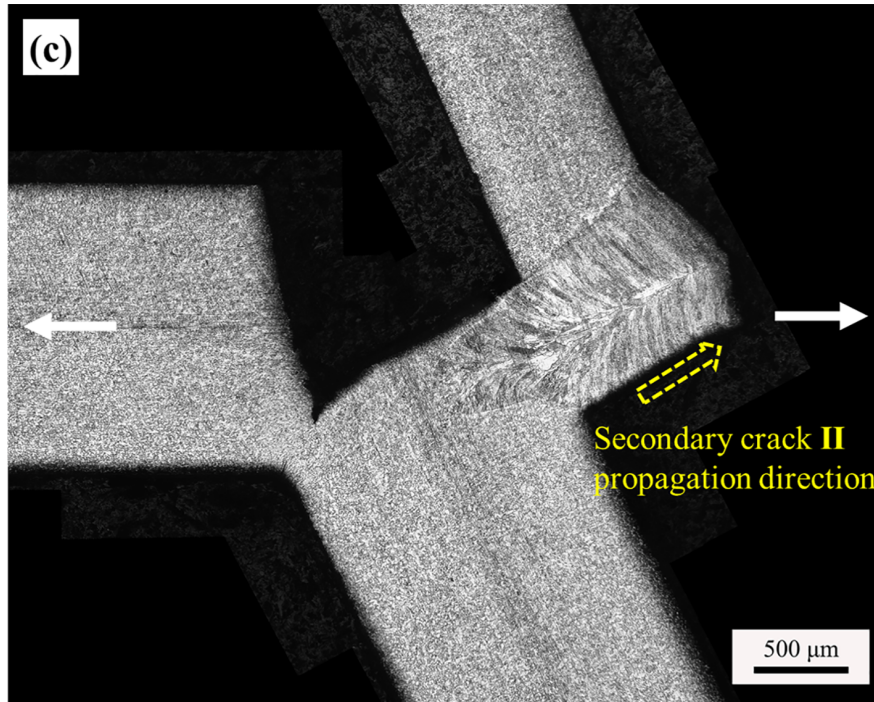
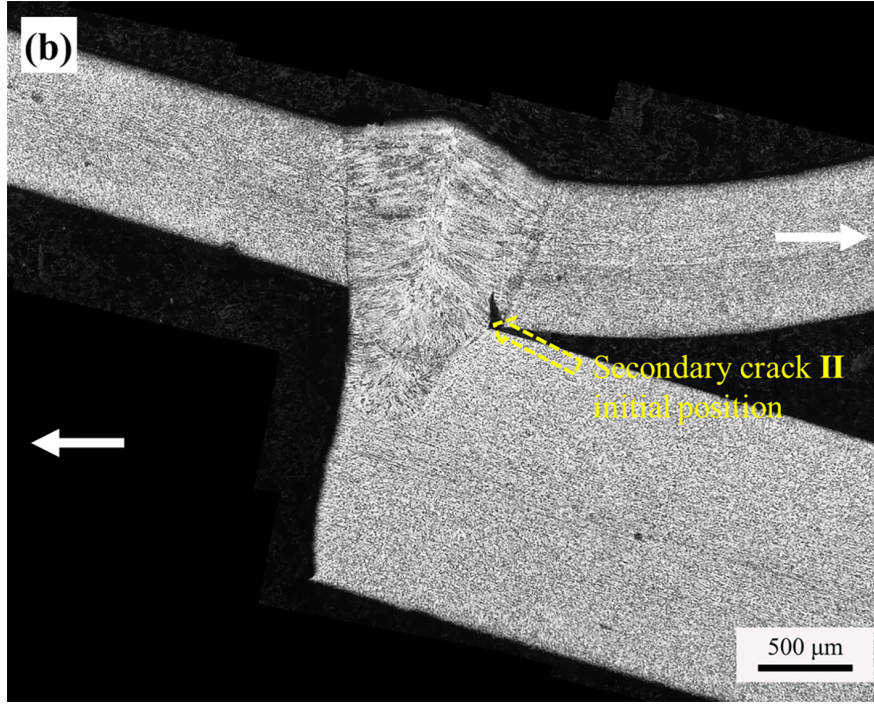
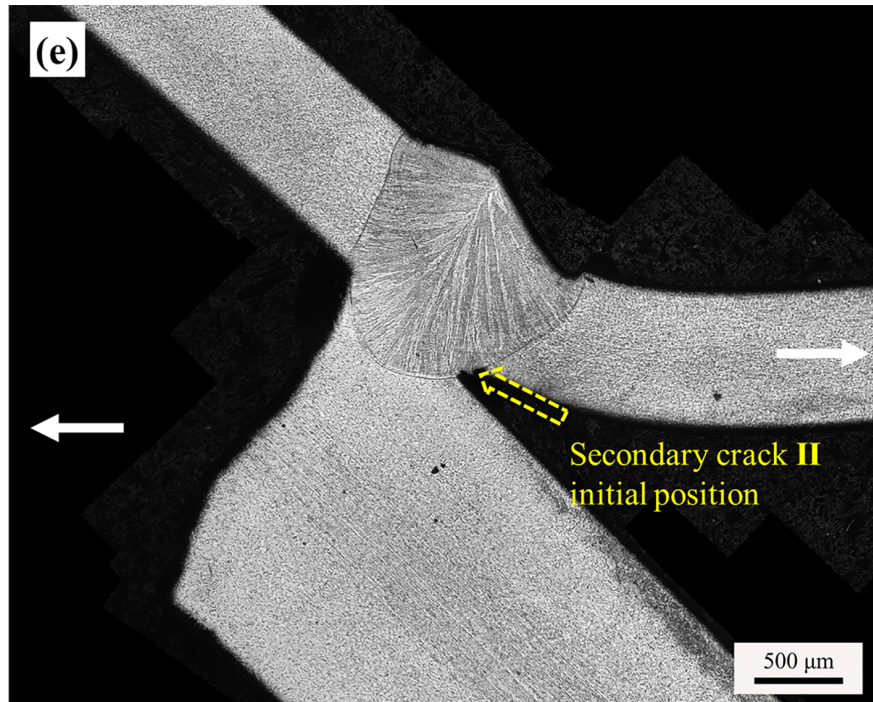
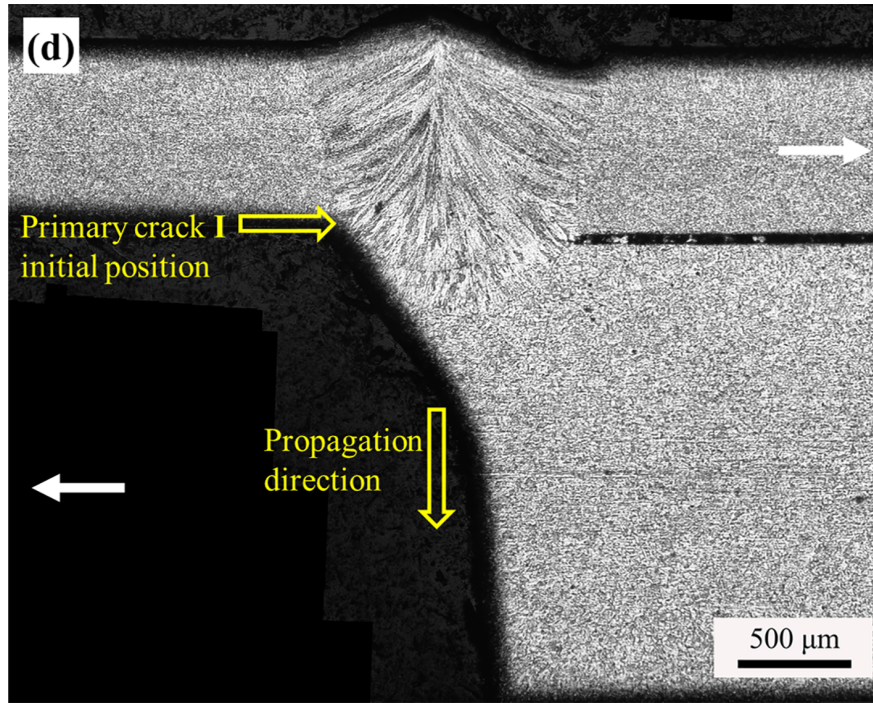


FIGURE 6 Cross-section micrographs of fatigue failure specimens: (a) 1.5+1.5 specimen run 2.0×10^6 cycles at 3.51 kN; (b) 1.5+1.5 specimen run 2.77×10^5 cycles at 6.94 kN; (c) 1.5+1.5 specimen run 7.5×10^3 cycles at 9.14 kN; (d) 2.0+2.0 specimen run 2.0×10^6 cycles at 4.58 kN; (e) 2.0+2.0 specimen run 2.11×10^5 cycles at 6.85 kN; (f) 2.0+2.0 specimen run 1.31×10^4 cycles at 10.96 kN

Figure 7 shows cross-section micrographs of fatigue failure 0.8+1.5 and 0.8+2.0 specimens under different fatigue loads. The fatigue fracture mode of 0.8+1.5 and 0.8+2.0 specimens depends on the fatigue load level. When the fatigue loads were less than 7.73 kN, the 0.8+1.5 specimens failed in the 1.5 mm bottom sheet, and the primary crack I was also initiated from the notch tip and propagated through the bottom sheet thickness, as shown in Figure 7 (a) and (b), even if the mean stress in the 0.8 mm top sheet was much higher. Similarly, when the fatigue loads of the 0.8+2.0 specimens were less than 7.22 kN, they failed at the 2.0 mm bottom sheet, as shown in Figure 7 (d) and (e). As the fatigue loads increase, in addition to the thicker bottom sheet fracture, the secondary crack II appeared in the top sheet and obvious plastic deformation was observed as shown in Figure 7 (b) and (e). When the fatigue loads were high enough, the fatigue fracture occurred in the thinner top sheets, as shown in Figure 7 (c) and (f), and the secondary crack II was propagated in the weld bead due to the welding geometry and became the primary crack resulting in the fracture of top sheet.







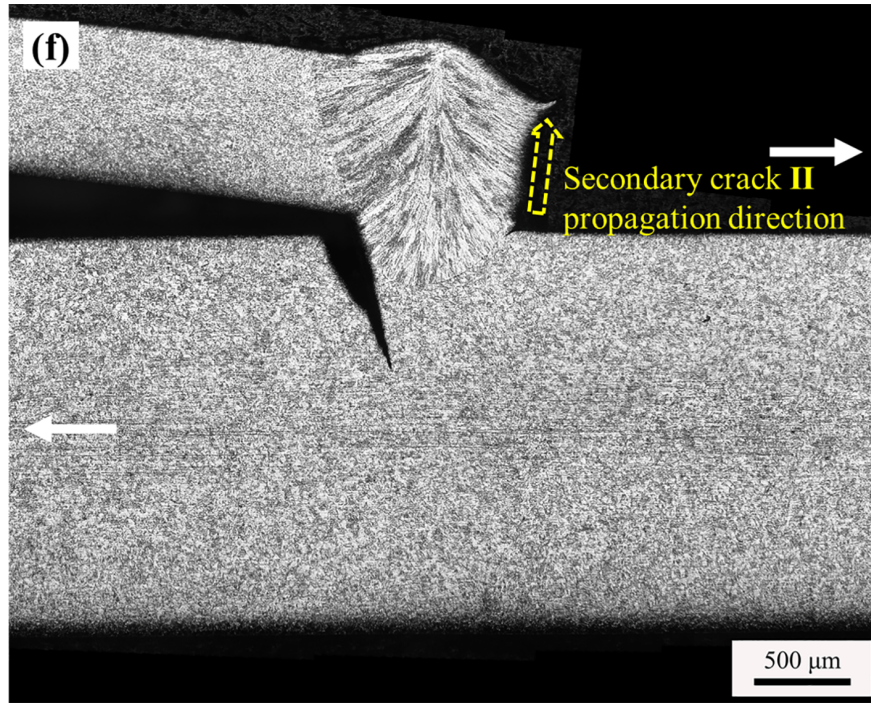


FIGURE 7 Cross-section micrographs of fatigue failure specimens: (a) 0.8+1.5 specimen run 2.0×10^6 cycles at 3.47 kN; (b) 0.8+1.5 specimen run 1.32×10^5 cycles at 4.96 kN; (c) 0.8+1.5 specimen run 1.44×10^4 cycles at 7.73 kN; (d) 0.8+2.0 specimen run 2.0×10^6 cycles at 4.29 kN; (e) 0.8+2.0 specimen run 1.37×10^5 cycles at 6.72 kN; (f) 0.8+2.0 specimen run 9.93×10^4 cycles at 7.22 kN

4 Fatigue data analysis

4.1 Traction stress calculation

The 2D finite element models with and without the angular distortion were developed to compare the calculation results. Below, take the 0.8+2.0 specimen as an example to describe the numerical procedure.

Figure 8 shows the finite element model without the angular distortion, and the geometric dimensions of the model were consistent with actual specimen shown in Figure 1. The detailed dimensions of the laser welds given in Table 2 were also considered in the model. The x and y degree of freedom was fixed for the left side of the specimen, while only y degree of freedom was fixed for the right side. Fatigue load was loaded on the right extremity of the specimen.

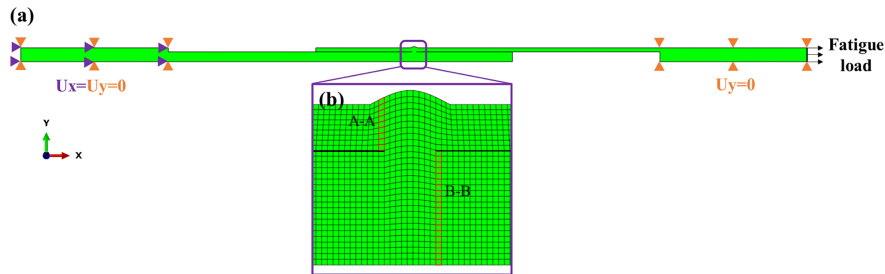


FIGURE 8 Finite element model without the angular distortion: (a) overall view of the model; (b) local view of the weld

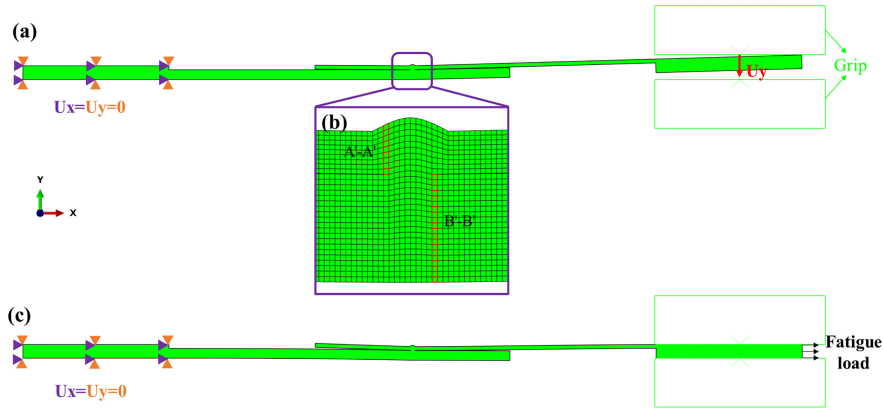


FIGURE 9 Finite element model with the angular distortion: (a) initial position of the specimen; (b) local view of the weld; (c) fatigue loading on the right side of the specimen

Figure 9 shows the finite element model with the angular distortion shown in Figure 4. The rigid bodies were used to simulate the boundary conditions imposed by the grip. The x and y degree of freedom was fixed for the left side of the specimen, and the right side was loaded in two steps. First, the grip was closed by applying a downward displacement to the rigid body, as illustrated in Figure 9 (a), which forces the rotation of the specimen. Second, the specimen was submitted to a tension fatigue load on the right side, in which the load was uniformly distributed across all nodes on the right extremity of the specimen, as illustrated in Figure 9 (c). The contacts between the welded sheets of the specimen and the grips were simulated using the contact pair “general contact” technique³⁰.

The finite element mesh of the model is presented in Figures 8 (b) and 9 (b), and the element type used here is 4-node bilinear plane strain elements. Nonlinear geometry effects were considered in order to account for pre-deformation effects introduced by the gripping actions²³. The laser weld metal and the base metal were assumed to be linear elastic with the Young’s modulus $E = 200$ GPa and the Poisson’s ratio $\nu = 0.3$. Computations were carried out using commercial finite element software ABAQUS.

Due to the initiation of fatigue crack on the geometric discontinuities of welded lap joints, the stress component directly output by the finite element model at the failure location cannot be directly used for fatigue assessment because of its singularity and mesh-sensitive³⁴. To overcome this limitation, a post-processing program was used to calculate the mesh-insensitive traction stress. The detailed steps are as follows²¹⁻²⁶:

1. Based on the actual failure position of the specimen, the hypothetical crack paths A-A and B-B shown in Figure 8 (b), as well as A'-A' and B'-B' shown in Figure 9 (b) were defined.
2. The nodal forces along the hypothetical crack path were extracted from the output of finite element analysis results, and the nodal forces were represented by NFORC in ABAQUS.
3. The membrane and bending traction stresses were calculated using the following formula:

Where F is nodal forces, t is thickness of sheet, σ_m is membrane traction stress, σ_b is bending traction stress, σ_t is traction stress.

To reflect the effects of fatigue load ratio, the membrane and bending traction stresses were calculated under minimum and maximum fatigue load. The equivalent traction stress range were calculated according to the 2007 ASME Div. 2 Code³⁵ using the following formula:

Where $\Delta\sigma$ is equivalent traction stress range, σ is the traction stress range, t is the dimensionless thickness, and r is bending ratio. t_0 is a reference thickness setting as 1 mm, was derived by using a two-stage crack growth model unifying both short and long crack growth behaviors³⁶.

4.2 Traction stress analysis

Figure 10 shows the equivalent traction stress of the two lap sheets at the fatigue crack initial position for four specimens with and without the angular distortion. For the 1.5+1.5 and 2.0+2.0 specimens, the equivalent traction stress of the bottom sheet is higher than that of the top sheet as shown in Figure 10 (a) and (b) due to the enhancement effect of the welding top humps⁷, and the stress difference between the bottom and top sheet with the distortion is larger than that without the distortion. The distribution of the equivalent traction stress in the specimens is consistent with their actual fatigue failure behavior.

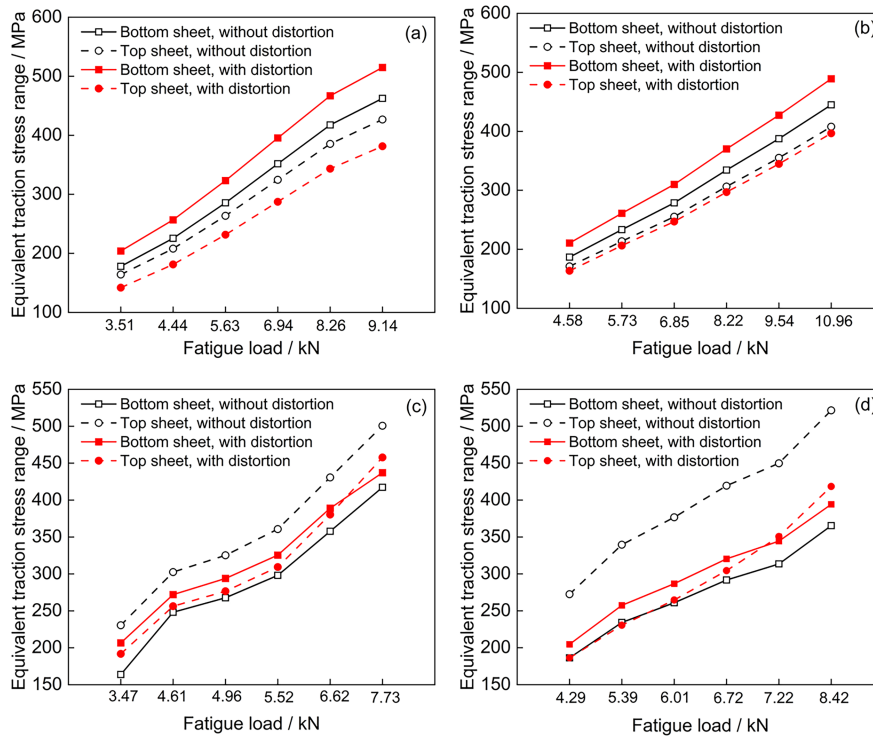


FIGURE 10 Equivalent traction stress of two lap sheets for the specimens with and without the angular distortion: (a) 1.5+1.5; (b) 2.0+2.0; (c) 0.8+1.5; (d) 0.8+2.0

For the 0.8+1.5 and 0.8+2.0 specimens, the equivalent traction stress of the thicker bottom sheet is much less than that of the thinner top sheet in the condition without the angular distortion, as shown in Figure 10 (c) and (d), which is inconsistent with the fatigue failure mode of both specimens. In the condition with the angular distortion, when the fatigue loads are less than 7.73 kN for 0.8+1.5 specimen and 7.22 kN for 0.8+2.0 specimen, the equivalent traction stress of the thicker bottom sheet is higher than that of the thinner top sheet, as shown in Figure 10 (c) and (d), which is consistent with the fatigue fracture of the thicker bottom sheet; when the fatigue loads are over these values, the equivalent traction stress of the thinner top sheet is

higher than that of the thicker bottom sheet, which is consistent with the fatigue fracture of the thinner top sheet. Consequently, the equivalent traction stress considering the effect of the angular distortion can well explain the changes of the fatigue failure mode of the specimens.

To understand that how the angular distortion affects traction stress, the stress concentration factor (SCF) of traction stress at the fatigue crack initial position was calculated by $\sigma_{max}/\sigma_{mean}$, where σ_{max} is the mean stress of the sheet. Figure 11 shows the SCF of the two lap sheets for the 2.0+2.0 and 0.8+2.0 specimens with and without the angular distortion. Comparatively speaking, the SCF with the distortion increases on the bottom sheet and decreases on the top sheet under all fatigue loads. During the clamping of the grips, the rotation of the distorted specimen resulted in compressive stress in the top sheet and tensile stress in the bottom sheet, at the initial position of the fatigue crack. This can also be used to explain why the equivalent traction stress of the 2.0 mm bottom sheet is higher than that of the 0.8 mm top sheet for the 0.8+2.0 specimen under low fatigue loads.

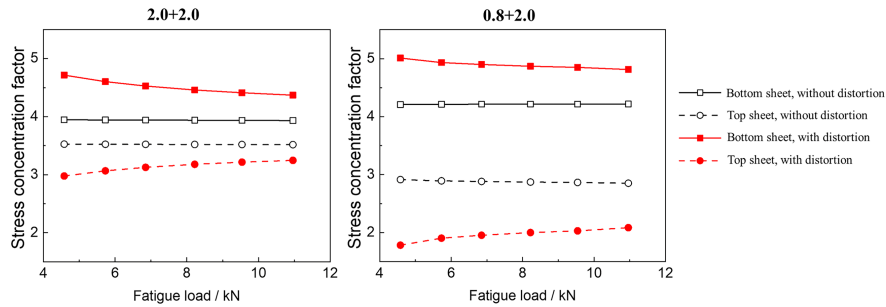


FIGURE 11 The SCF of two lap sheets for 2.0+2.0 and 0.8+2.0 specimens with and without the angular distortion

With the angular distortion, the SCF decreases on the bottom sheet and increases on the top sheet with the increase of the fatigue load, as shown in Figure 11, which indicates the effect of the pre-stress caused by angular distortion on traction stress is weakened that is similar to the results of Ref [30] and [37]. When the fatigue load of the 0.8+2.0 specimen is high enough, the applied stress dominates over the pre-stress caused by angular distortion; therefore, the equivalent traction stress of the 0.8 mm top sheet is higher than that of the 2.0 mm bottom sheet.

4.3 Structural strain approach

Figure 12 shows the comparison between the equivalent traction stress of fatigue fracture sheet with the angular distortion and the master S-N curve which frequently used for fatigue evaluation of fusion welded structures³⁵. The equivalent traction stress at high-cycle fatigue regime ($>10^6$) correlates reasonably with the master S-N curve, while the equivalent traction stress at low-cycle fatigue regime is below the master S-N curve and forms a rather flat scatter band.

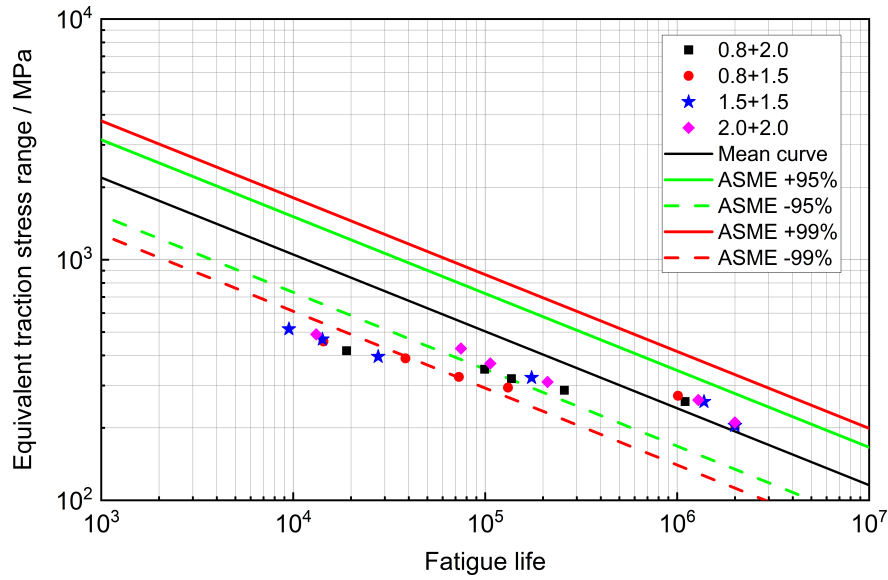


FIGURE 12 Fatigue data of the laser welded lap joints with the master S-N curve

In fact, the equivalent traction stress has exceeded the yield limit of the cold-rolled 301LN sheet and led to plastic deformation, when the fatigue life is less than 10^5 cycles, as shown in Figure 12. This may be the reason why the equivalent traction stress is below the master S-N curve scatter band at low-cycle fatigue regime. The structural strain approach introduced by Dong²⁷ can capture the plastic deformation effect in welded structures to reasonably evaluate fatigue behaviors. The structural strain values were calculated by the traction stresses σ_m and σ_b and stress-strain data of the base metal in Ref [38], and the numerical procedure was given in Ref [39].

A plate section corresponding fractured sheet thickness was developed using the plane-strain element as shown in Figure 13. The element size of the model is $0.05 \times t$ and the element type used here is 4-node bilinear plane strain elements. All displacements and rotations of the superficial nodes on the left side were restricted, and the membrane traction stress σ_m and bending traction stress σ_b were loaded on the right extremity of the specimen.

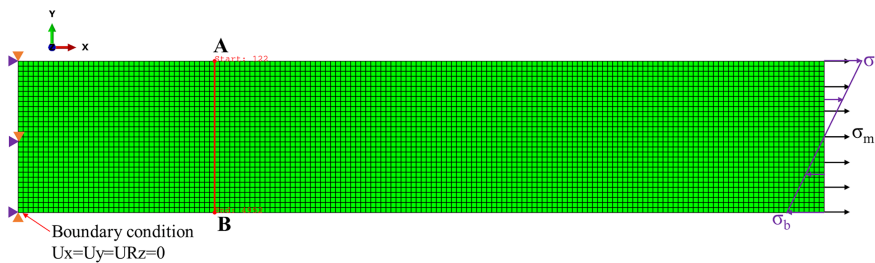


FIGURE 13 Finite element model used to calculate the structural strain

The membrane and bending parts of the structural strain can be calculated using the following formula^{39,40}:

Where ϵ_A and ϵ_B are the strain at A and B point shown in Figure 13, and the strain can be obtained by extracting the E11 from the finite element analysis result.

The equivalent structural strain range can be calculated using the following formula^{40,41}:

Where ϵ_{eq} is the equivalent structural strain range, ϵ is the structural strain range, and r is bending ratio. The thickness term t , is the same as Equations (4)-(7).

Figure 14 shows the comparison between the equivalent structural strain of the fatigue fracture sheets and ASME master E-N curve in Ref [39-41], and all these data fall into the master E-N curve scatter band. The structural strain approach can capture the plastic deformation effect in welded structures, so the fatigue data can be effectively correlated with the master E-N curve. This indicates that the structural strain approach in conjunction with the master E-N curve is suitable for correlating both low- and high-cycle fatigue data of the non-penetrating laser welded lap specimens.

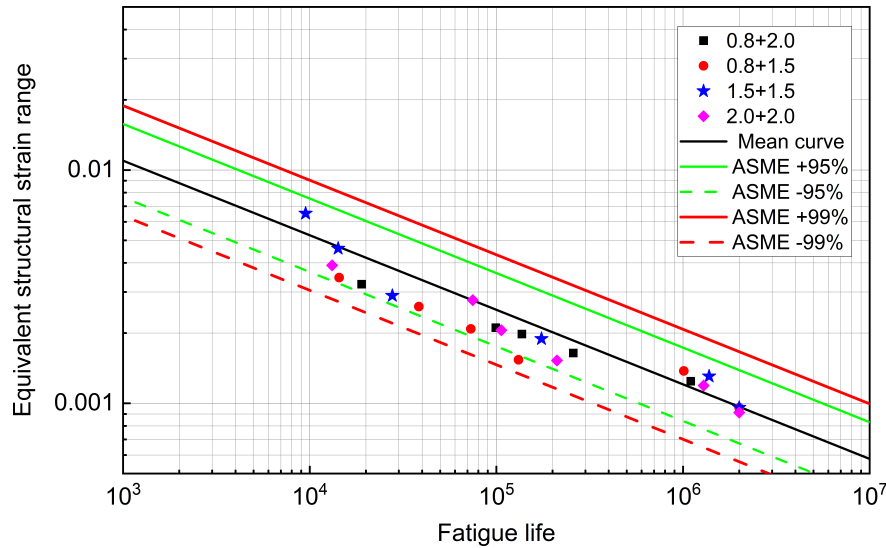


FIGURE 14 Fatigue data of the laser welded lap joints with the master E-N curve

5 Conclusions

In this work, the fatigue behaviors of non-penetrating laser welded lap specimens of 301LN stainless steel were investigated, and the traction stress was calculated based on finite element models with and without the angular distortion to study the effect of the distortion on the fatigue fracture behaviors, the structural strain approach was then used to correlate the fatigue data. The following conclusions are drawn:

1. Non-penetrating laser welded lap specimens exhibited angular distortions, in which the two welded sheets tilted upward less than 1° from the welding center, and the tilt angle decreased with the increase of the sheet thickness.
2. The equal-thickness specimens of 1.5+1.5 and 2.0+2.0 failed in the bottom sheets over the whole cycle life. The unequal-thickness specimens of 0.8+1.5 and 0.8+2.0 failed in the thicker bottom sheets when their fatigue loads were less than 7.73 kN and 7.22 kN, respectively, while if the loads were over these values, the failure location changed from the thicker bottom sheet to the thinner top sheet. The primary crack was initiated from the notch tip and propagated through the fractured sheet thickness.
3. During the clamping stage, the rotation of the distorted specimen resulted in compressive stress in the top sheet and tensile stress in the bottom sheet, at the initial position of the fatigue crack. This leads to a higher equivalent traction stress at the bottom sheet than the top sheet for all specimens with low fatigue loads. When the fatigue loads are high enough, the applied stress dominates over the pre-stress caused by angular distortion. Therefore, the equivalent traction stress of the thinner top sheet is higher than that of the thicker bottom sheet for unequal-thickness specimens. The equivalent traction stress

calculated by taking account the angular distortion effect is consistent with the fatigue failure location in the experiment.

4. At low-cycle fatigue regime, the equivalent traction stress representation of fatigue data is below the ASME master S-N curve scatter band since the stress exceeds the yield limit of the base metal and leads to plastic deformation. By using the structural strain approach, the plastic deformation effect is taken account and all fatigue data fall into ASME master E-N curve scatter band. This indicates that the structural strain approach in conjunction with the master E-N curve is suitable for correlating both low- and high-cycle fatigue data of the non-penetrating laser welded lap specimens.

Conflict of Interest

The author declares that there is no conflict of interest that could be perceived as prejudicing the impartiality of the research reported.

Acknowledgement

The authors thank CSR Qingdao Sifang Corporation for their help with the welding process.

Funding

This work was supported by the scientific research and development projects of China Railway Corporation [grant numbers 2017J011-C].

ORCID

Xiangzhong Guo <https://orcid.org/0000-0002-0641-9991>

Wei Liu <https://orcid.org/0000-0002-4640-206X>

Reference

1. W. Jaxa-Rozen, Cold-worked austenitic stainless steels in passenger railcars and in other applications, *Thin-Walled Structures*, 83(2014) 190-199.
2. H.L. Luo, G.Z. Kang, Q.H. Kan, Y. Huang, Experimental investigation on the heterogeneous ratcheting of SUS301L stainless steel butt weld joint during uniaxial cyclic loading, *International Journal of Fatigue*, 105(2017) 169-179.
3. W. Liu, H.L. Fan, X.Z. Guo, Z.H. Huang, X.H. Han, Mechanical properties of resistance spot welded components of high strength austenitic stainless steel, *Journal of Material Science and Technology*, 32(2016) 561-565.
4. W. Liu, R.J. Wang, J.L. Han, X.Y. Xu, Q. Li, Microstructure and mechanical performance of resistance spot-welded cold-rolled high strength austenitic stainless steel, *Journal of Materials Processing Technology*, 210(2010) 1956-1961.
5. Hong K-M, Shin YC. Prospects of laser welding technology in the automotive industry: A review. *Journal of Materials Processing Technology*, 245(2017) 46-69.
6. C. Cerrone, F. Chiti, M. Sacchi, M. Fersini, C. Pietrosanti, Application of laser welding to stainless steel light rail vehicle, *Welding in the World*, 52(2008) 27-32.

7. K. Asim, K. Sripichai, J. Pan, Fatigue behavior of laser welds in lap-shear specimens of high strength low alloy steel sheets, *International Journal of Fatigue*, 61(2014) 283-296.
8. M. Ono, M. Kabasawa, M. Omura, Static and fatigue strength of laser-welded lap joints in thin steel sheet, *Welding International*, 11(1997) 462-467.
9. R.A. Sindhu, M.K. Park, S.J. Lee, K.D. Lee, Effects of residual stresses on the static and fatigue strength of laser-welded lap joints with different welding speeds, *International Journal of Automotive Technology*, 11(2010) 857-863.
10. Frank D., Remes H., Romanoff J., On the slope of the fatigue resistance curve for laser stake-welded T-joints, *Fatigue & Fracture of Engineering Materials & Structures*, 36(2013) 1336-1351.
11. Radaaj D, Sonsino C M, Fricke W. Recent developments in local concepts of fatigue assessment of welded joints, *International Journal of Fatigue*, 31(2009) 2-11.
12. Chris Hsu, Charles E Albright, Fatigue analysis of laser welded lap joints, *Engineering Fracture Mechanics*, 39(1991) 575-580.
13. Zhang S, Stress in laser welded lap joints determined by outer surface strains. *Welding Journal*, 81(2002) 14-18.
14. G. Marulo, J. Baumgartner, F. Frenzo, Fatigue strength assessment of laser welded thin-walled joints made of mild and high strength steel, *International Journal of Fatigue*, 96(2017) 142-151.
15. Baumgartner J, Review and considerations on the fatigue assessment of welded joints using reference radii, *International Journal of Fatigue*, 101(2017) 459-468.
16. Jorg Baumgartner, Adolf F. Hobbacher, Roland Rennert, Fatigue assessment of welded thin sheets with the notch stress approach - Proposal for recommendations, *International Journal of Fatigue*, 140(2020) 105844.
17. Wang PC. Fracture mechanics parameter for the fatigue resistance of laser welds. *International Journal of Fatigue*, 17(1995) 25-34.
18. Sripichai K, Asim K, Pan J. Stress intensity factor solutions for estimation of fatigue lives of laser welds in lap-shear specimens, *Engineering Fracture Mechanics*, 78(2011) 1424-1440.
19. Shin-Jang Sung, Jwo Pan, Further investigation of stress intensity factor solutions for similar and dissimilar welds in lap-shear specimens under clamped loading conditions, *Engineering Fracture Mechanics*, 166(2016) 60-81.
20. Dong P, A structural stress definition and numerical implementation for fatigue analysis of welded joints, *International Journal of Fatigue*, 23(2001) 865-876.
21. Wang P, Pei X, Dong P, Song S, Traction structural stress analysis of fatigue behaviors of rib-to-deck joints in orthotropic bridge deck, *International Journal of Fatigue*, 125 (2019) 11-22.
22. Wang P, Pei X, Dong P, Yu Y, Li X, Analysis of weld root fatigue cracking in load-carrying high-strength aluminum alloy cruciform joints, *International Journal of Fatigue*, 139(2020) 105735.
23. Xing S, Dong P, An analytical SCF solution method for joint misalignments and application in fatigue test data interpretation, *Marine Structures*, 50(2016) 143-161.
24. Zhou W, Dong P, Pei X, Karakas O, Li X, Evaluation of magnesium weldment fatigue data using traction and notch stress methods, *International Journal of Fatigue*, 138(2020) 105695.
25. Dong P, Zhou W, Xing S, An analytical method for interpreting distortion effects on fatigue test results of thin plate panel specimens, *Welding in the World*, 63(2019), 1707-1714.
26. Yu Y, Wang P, Pei X, Dong P, Fang H, Fatigue resistance characterization of frictions stir welds between complex aluminum extrusions: an experimental and finite element study, *International Journal of Fatigue*, 141(2020) 105861.
27. Dong P, Pei X, Xing S, Kim MH, A structural strain method for low-cycle fatigue evaluation of welded components, *International Journal of Pressure Vessels and Piping*, 119(2014) 39-51.
28. Murakawa H, Residual stress and distortion in laser welding, In: Katayam Seiji, editor, *Handbook of Laser Welding Technologies*, Cambridge: Woodhead Publishing, 2013, p. 374-400.
29. Huang ZY, Luo Z, Liu ZM, Li Y, Cai YC, Zhang Y, Deformation behaviour of thin aluminium alloy plates during laser welding, *Lasers in Engineering*, 37(2017) 291-309.
30. P.I. Oliveira, F.V. Antunes, A. Loureiro, J.M. Costa, Effect of the angular misalignment of laser welded

- T-joints on fatigue curves, *International Journal of Fatigue*, 128(2019) 105180.
31. N.T. Nguyen, M.A. Wahab, The effect of undercut, misalignment and residual stresses on the fatigue behaviour of butt welded joints, *Fatigue & Fracture of Engineering Materials & Structures*, 19(1996) 769-778.
 32. Lillemae I, Lammi H, Molter L, Remes H, Fatigue strength of welded butt joints in thin and slender specimens, *International Journal of Fatigue*, 44(2012) 98-106.
 33. Liinalampi S, Remes H, Lehto P, Lillemae I, Romanoff J, Porter D, Fatigue strength analysis of laser-hybrid welds in thin plate considering weld geometry in microscale, *International Journal of Fatigue*, 87(2016) 143-152.
 34. Wei Z, Jin H, Chen G, Traction structural stress analysis of fatigue behaviors of girth butt weld within welded cast steel joints, *International Journal of Pressure Vessels and Piping*, 179(2020) 104027.
 35. Dong P, Hong JK, Osage DA, Dewees DJ, Prager M, The master S-N curve method an implementataion for fatigue evaluation of welded components in the ASME B&PV code, Section VIII, Division 2 and API 579-1/ASME FFS-1. *Weld Research Council Bulletin*; 2010; 523.
 36. Dong P, Hong JK, Cao Z, Stresses and stress intensities at notches: ‘anomalous crack growth’ revisited, *International Journal of Fatigue*, 25(2003) 811-825.
 37. Fricke W, Remes H, Feltz O, Lillemae I, Tchuindjang D, Reinert T, Nevierov A, Sichermann W, Brinkmann M, Kontkanen T, Bohlmann B, Molter L, Fatigue strength of laser-welded thin-plate ship structures based on nominal and structural hot-spot stress approach, *Ships and Offshore Structures*, 10(2015) 39-44.
 38. Guo X, Liu W, Wang C, Liu H, Fan J, Numerical analysis of elastic-plastic deformation evolution and fracture behavior in tensile process of laser lap welded 301L joints, *Chinese Journal of Lasers*, 45(2018) 1202003.
 39. Pei X, Dong P, An analytically formulated structural strain method for fatigue evaluation of welded components incorporating nonlinear hardening effects, *Fatigue & Fracture of Engineering Materials & Structures*, 42(2018) 239-255.
 40. Pei X, Dong P, Xing S, A structural strain parameter for a unified treatment of fatigue behaviors of welded components, *International Journal of Fatigue*, 124(2019) 444-460.
 41. Pei X, Dong P, Kim M H, A simplified structural strain method for low-cycle fatigue evaluation of girth-welded pipe components, *International Journal of Fatigue*, 139(2020) 105732.

